

SPITZER 70/160 μm OBSERVATIONS OF HIGH-REDSHIFT ULIRGs AND HyLIRGs IN THE BOÖTES FIELD

KRYSTAL D. TYLER¹, EMERIC LE FLOC’H^{1,2,15}, GEORGE H. RIEKE¹, ARJUN DEY³, VANDANA DESAI⁴, KATE BRAND^{5,16},
COLIN BORYS⁶, BUELL T. JANNUZI³, LEE ARMUS³, HERVE DOLE⁷, CASEY PAPOVICH^{1,8,15}, MICHAEL J. I. BROWN⁹,
MYRA BLAYLOCK¹, SARAH J. U. HIGDON¹⁰, JAMES L. HIGDON¹⁰, VASSILIS CHARMANDARIS^{11,12,13}, MATTHEW L. N. ASHBY¹⁴,
AND HOWARD A. SMITH¹⁴

¹ Steward Observatory, University of Arizona, 933 North Cherry Avenue, Tucson, AZ 85721, USA

² Institute for Astronomy, University of Hawaii, 2680 Woodlawn Dr., Honolulu, HI 96822, USA

³ National Optical Astronomy Observatory, 950 North Cherry Avenue, Tucson, AZ 85726, USA

⁴ California Institute of Technology, Division of Physics, Mathematics, and Astronomy, MS 320-47, Pasadena, CA 91125, USA

⁵ Space Telescope Science Institute, 3700 San Martin Drive, Baltimore, MD 21218, USA

⁶ California Institute of Technology, 1200 E California Blvd., MS 100-22, Pasadena, CA 91125, USA

⁷ Institut d’Astrophysique Spatiale, Université Paris Sud, F-91405 Orsay Cedex, France

⁸ Department of Physics, Texas A&M University, 4242 TAMU, College Station, TX 77843-4242, USA

⁹ School of Physics, Monash University, Clayton, Victoria 3800, Australia

¹⁰ Department of Physics, Georgia Southern University, P.O. Box 8031, Statesboro, GA 30460, USA

¹¹ Department of Physics, University of Crete, GR-71003 Heraklion, Greece

¹² IESL/Foundation for Research and Technology-Hellas, GR-71110, Heraklion, Greece

¹³ Chercheur Associé, Observatoire de Paris, F-75014, Paris, France

¹⁴ Harvard-Smithsonian Center for Astrophysics, 60 Garden Street, Cambridge, MA 02138, USA

Received 2007 September 4; accepted 2008 September 19; published 2009 February 12

ABSTRACT

We present new 70 and 160 μm observations of a sample of extremely red ($R - [24] \gtrsim 15$ mag), mid-infrared bright, high-redshift ($1.7 \lesssim z \lesssim 2.8$) galaxies. All targets detected in the far-infrared exhibit rising spectral energy distributions (SEDs) consistent with dust emission from obscured active galactic nuclei (AGNs) and/or star-forming regions in luminous IR galaxies (LIRGs). We find that the SEDs of the high-redshift sources are more similar to canonical AGN-dominated local ultraluminous IR galaxies (ULIRGs) with significant warm dust components than to typical local star-forming ULIRGs. The inferred IR (8–1000 μm) bolometric luminosities are found to be $L_{\text{bol}} \sim 4 \times 10^{12} L_{\odot}$ to $\sim 3 \times 10^{13} L_{\odot}$ (ULIRGs/hyperluminous IR galaxies (HyLIRGs)), representing the first robust constraints on L_{bol} for this class of object.

Key words: dust, extinction – galaxies: active – galaxies: high-redshift – galaxies: photometry – galaxies: starburst – infrared: galaxies

Online-only material: color figures

1. INTRODUCTION

The *Spitzer Space Telescope* (Werner et al. 2004) has revealed a large number of luminous, ultraluminous, and hyper-luminous infrared galaxies¹⁷ (LIRGs, ULIRGs, and HyLIRGs) out to $z \sim 3$. These objects have some of the highest IR luminosities known, sometimes exceeding $10^{13} L_{\odot}$. Initially studied at mid-infrared (mid-IR) wavelengths from the ground by Rieke & Low (1972), this class of source has since been studied and cataloged using facilities such as *IRAS*, the *Infrared Space Observatory* (*ISO*), *SCUBA*, and *Spitzer* (Soifer et al. 1987; Smail et al. 1997; Blain et al. 1999; Elbaz et al. 1999; Dole et al. 2001; Farrah et al. 2003; Serjeant et al. 2004; Le Floch et al. 2005; Brand et al. 2007). While rare in the nearby universe, they contribute significantly to the cosmic infrared background (CIRB) and star formation density at high redshifts (Chary & Elbaz 2001; Franceschini et al. 2001; Blain et al. 2002; Lagache et al. 2003).

To better understand galaxy evolution, especially the high-redshift stages, we need to better understand these IR-luminous sources. Despite their importance at high redshifts, the role of

IR-luminous galaxies in the evolution of stars and supermassive black holes in galaxies at $z \gtrsim 1$ has been poorly constrained so far due to the difficulty in identifying and characterizing them. The sensitivity of *ISO* has limited our view of these sources to $z \sim 1$ (Flores et al. 1999; Aussel et al. 1999). Millimeter and submillimeter observations, such as those obtained with *SCUBA* and *MAMBO*, reach higher redshifts but are only sensitive to the extreme bright end of the luminosity function and are biased toward colder galaxies due to selection at 850 μm in the Rayleigh–Jeans regime (Chapman et al. 2003, 2005; Egami et al. 2004; Pope et al. 2006).

With its superb sensitivity, *Spitzer* offers a new view into the properties of IR-luminous sources up to redshifts of $z \sim 3$ and down to lower luminosities than previously reached. Many groups are exploring a variety of methods to identify active galactic nuclei (AGNs), particularly red ones, using the *Spitzer* data (e.g., Donley et al. 2005, 2007; Polletta et al. 2006; Lacy et al. 2004; Stern et al. 2005; Alonso-Herrero et al. 2006; Sajina et al. 2008). However, it must be noted that the *Spitzer* studies of high-redshift sources have so far mostly focused on their emission in the rest-frame mid-IR, where the instruments are most efficient. This can be problematic, since estimations of the bolometric luminosities of these sources rely on extrapolations of the spectral energy distributions (SEDs) to longer wavelengths. The extrapolations are quite uncertain for very luminous galaxies, for which the overall IR SED can

¹⁵ *Spitzer* Fellow.

¹⁶ Giacconi Fellow.

¹⁷ LIRGs: $10^{11} L_{\odot} \lesssim L_{\text{IR}} \lesssim 10^{12} L_{\odot}$, ULIRGs: $10^{12} L_{\odot} \lesssim L_{\text{IR}} \lesssim 10^{13} L_{\odot}$, and HyLIRGs: $L_{\text{IR}} \gtrsim 10^{13} L_{\odot}$, respectively, where L_{IR} is determined from 8 to 1000 μm .

vary drastically from source to source (Armus et al. 2006). Far-infrared (far-IR) data are needed to constrain the shape of the SEDs, not only for estimating the IR luminosities but also for more in-depth study of the source(s) of the IR emission.

This paper reports far-IR (70 and 160 μm) measurements of one of the most elusive subsets of these galaxies: objects with extremely high mid-IR luminosity but that are exceptionally faint in the observed visible region, located at high redshift ($1.7 \lesssim z \lesssim 2.8$) (Houck et al. 2005; Yan et al. 2005; Weedman et al. 2006; Brand et al. 2007; Dey et al. 2008; Desai et al. 2008). Assuming the high-redshift objects have similar SEDs as nearby objects with similar AGNs and star-forming components, we estimate the roles of these components in the high-redshift objects from fitting the low-redshift SEDs. In Section 2 we discuss our sample and the data reduction. Section 3 covers comparisons of our source SEDs with nearby analogues and estimates of the total IR luminosities of our sources. We discuss the results and implications of our analysis in Section 4. In analyzing their properties, we assume the cosmological parameters $H_0 = 70 \text{ km s}^{-1} \text{ Mpc}^{-1}$, $\Omega_M = 0.3$, and $\Omega_\Lambda = 0.7$.

2. SAMPLE AND DATA REDUCTION

The National Optical Astronomy Observatory (NOAO) Deep Wide Field Survey (NDWFS; Jannuzi & Dey 1999) is a deep optical and near-infrared (near-IR) survey of two 9.3 square-degree fields in the northern and southern hemispheres. Both fields were selected to cover areas of low-background (cirrus) emission and low H I column depth. The regions have been observed at a wide range of wavelengths: optical (B_W , R , I), radio, X-ray, and IR. The large area of this survey is well-suited for observations of rare objects at the bright end of the luminosity function, such as luminous IR galaxies, due to the large comoving volume that is sampled.

Boötes, the northern field of the NDWFS, was observed in a shallow survey using the Multiband Imaging Photometer for *Spitzer* (MIPS; Rieke et al. 2004). Combining these data with the deep optical imaging of the field, a population of sources was identified, characterized by very red optical-to-mid-IR flux ratios ($R - [24] \gtrsim 15$)¹⁸ (Yan et al. 2004; Dey et al. 2008). These objects are faint in the optical but bright at 24 μm , suggestive of highly-obscured, distant IR-luminous galaxies. Although they are relatively rare (space densities comparable to unobscured quasars of similar luminosity), they could play a major role in galaxy evolution, given the very large IR luminosities inferred from their mid-IR emission. Dey et al. (2008) conclude that the class of dust-obscured galaxies (DOGs), which includes our sources, constitute the majority of ULIRGs at $z \sim 2$. Because of the extreme faintness of these sources at optical wavelengths, existing studies have focused on objects with 24 μm flux densities brighter than $\sim 1 \text{ mJy}$, for which it is possible to obtain mid-IR InfaRed spectrograph (IRS) spectra in reasonable amounts of time (Houck et al. 2004, 2005; Weedman et al. 2006). Consequently, this population has only been characterized at the very bright end of the mid-IR luminosity function. Redshifts ranging from $z \sim 1.7$ to $z \sim 2.8$ were estimated by fitting the 9.7 μm silicate absorption feature or the 7.7 μm aromatic feature (Houck et al. 2005; Desai et al. 2008). Such sources lie at similar redshifts to the SCUBA galaxies (Chapman et al. 2003, 2005; Egami et al. 2004; Pope et al. 2006). Being ~ 5 to 10 times more luminous at 24 μm than the submillimeter-

selected objects, the dust-obscured galaxies are among the most luminous mid-IR sources observed in the distant universe.

Given the sensitivity limits of MIPS in the far-IR, these sources were not detected in the shallow far-IR (70 and 160 μm) coverage of the Boötes field. Here, we report observations¹⁹ ~ 4 times deeper than the shallow survey with MIPS at 70 and 160 μm of 20 sources generally representative of this sample of very red objects. Of the objects observed, 11 have IRS spectra and known redshifts. There are additional 12 sources with power-law IRS spectra with no obvious spectral features. All but one of these latter sources from Weedman et al. (2006) have unknown redshifts, though we still include them in our sample. They will be discussed in more detail in later sections. For the majority of this paper, we will focus on the 11 sources for which we have redshifts, IRS spectra, and deep 70 and 160 μm observations.

The data from these observations were reduced using version 3.06 of the MIPS Data Analysis Tool (DAT; Gordon et al. 2007). In addition to the standard processing discussed in that paper, additional corrections for the 70 μm data were applied as described by Gordon et al. (2007). We measured the flux density of each source at 70 and 160 μm using the point-spread function (PSF) fitting routine ALLSTAR in the IRAF²⁰ environment. At 70 μm we chose a source aperture (radius) of 16'' and sky annulus of 39''–65'' and made an aperture correction for the flux lost in the wings of the PSF (Gordon et al. 2007). Similar procedures were used at 160 μm , with a source aperture radius of 30'', a sky annulus of 32''–56'', and correction for the lost signal as described by Stansberry et al. (2007). Errors were estimated by measuring background flux in apertures outside the source PSF but inside the area of the image with complete coverage (full exposure). Upper limits for undetected sources were estimated at the 3σ noise level. These measurements are summarized in Table 1.

3. ANALYSIS

We created SEDs for the 11 sources with known redshifts using our measured 70 and 160 μm flux densities, IRS and 24 μm data from Houck et al. (2005), IRAC (3.6, 4.5, 5.8, and 8.0 μm) data from Eisenhardt et al. (2004), optical (B_W , R , and I , where available) from B. T. Jannuzi et al. (2008, in preparation) and Brown et al. (2007), and 20 cm flux densities from the Boötes field measurements by de Vries et al. (2002). Additional data points at 12 and 18 μm (observed-frame) are estimated from the IRS spectra. The 850 μm upper limits were calculated using the relation

$$f_\nu(850 \mu\text{m}) = 2.59 f_\nu(1.4 \text{ GHz})(1+z)^{3.15} \quad (1)$$

from Condon (1992), Yun & Carilli (2002), Seymour et al. (2008), and Rieke et al. (2009) between the observed-frame 1.4 GHz and 850 μm flux densities. This is a specific form of the radio/IR relation adapted to measurements of high-redshift ULIRGs and calculated from local ULIRG templates. All upper limits are plotted at the 3σ level except for the optical points, which are plotted as 2σ upper limits. SEDs for our sources are displayed in Figures 1–3.

¹⁹ *Spitzer* General Observer PID 20303.

²⁰ IRAF is distributed by the NOAO, which is operated by the Association of Universities for Research in Astronomy, Inc., under cooperative agreement with the National Science Foundation.

¹⁸ Here, [24] denotes the Vega-based magnitude of the 24 μm emission.

Table 1
Source Data

Source	Data Set ^a	Name ^b	IRS ^c	<i>z</i>	α^d	F24 μm (mJy)	F70 μm (mJy)	F160 μm (mJy)	F20 cm ^e (mJy)
1	H05-13	SST24 J143644.22+350627.4	31	1.95	...	2.30	9.1 ± 2.5	43 ± 12	5.09 ± 0.21
2	D06-22	SST24 J143546.13+352447.2	1.0	0.99	*	*	...
3	D06-11	SST24 J143253.39+334844.3	0.4	1.40	9.9 ± 2.7	< 40	...
4	H05-9	SST24 J143001.91+334538.4	8	2.46	...	3.83	9.3 ± 2.3	65 ± 11	0.42 ± 0.04
5	H05-8	SST24 J143539.34+334159.1	7	2.62	...	2.65	< 8.1	< 38	< 0.15
6	D06-6	SST24 J143308.62+333401.7	1.8	2.40	~ 9**	*	...
7	H05-1	SST24 J142958.33+322615.4	19	2.64	...	1.24	< 9.2	61 ± 13	< 0.15
9	H05-17	SST24 J143504.12+354743.2	18	2.13	...	1.23	10.8 ± 2.6	< 43	< 0.15
10	H05-5	SST24 J142804.12+332135.2	4	2.34	...	0.87	< 9.4	< 51	< 0.15
11	D06-4	SST24 J143318.59+332127.0	1.0	0.91
12	D06-24	SST24 J142939.18+353558.4	-0.1	1.05	< 9.7	< 46	...
14	H05-16	SST24 J142924.83+353320.3	16	2.73	...	1.04	< 8.1	< 47	< 0.15
15	...	142931.36+321828.2	< 9.3	38 ± 10	...
16	D06-23	SST24 J142850.94+353146.6	...	2.0	1.4	0.98	5.2 ± 2.4	56 ± 15	...
17	H05-15	SST24 J142645.71+351901.4	...	1.75	...	1.05	5.4 ± 2.2	31 ± 13	< 0.15
19	H05-12	SST24 J142626.49+344731.2	12	2.13	...	1.12	< 9.1	46 ± 12	0.20 ± 0.04
21	D06-16	SST24 J143429.56+343633.1	2.0	2.29
24	D06-10	SST24 J142827.95+334550.3	0.9	0.82
25	D06-9	SST24 J143424.50+334543.3	1.7	0.88
26	D06-8	SST24 J142920.47+334400.7	1.7	0.92
27	D06-7	SST24 J143053.14+334332.3	-0.6	0.87	< 9.7	< 53	...
28	H05-7	SST24 J143251.82+333536.3	23	1.78	...	0.78	< 8.3	25 ± 11	< 0.15
29	D06-5	SST24 J142644.34+333052.0	1.3	1.12	< 8.7	47 ± 13	...
30	H05-4	SST24 J143523.99+330706.8	21	2.59	...	1.08	< 8.5	< 51	0.24 ± 0.05
31	H05-2	SST24 J142653.23+330220.7	20	1.86	...	0.89	9.1 ± 2.7	41 ± 16	< 0.15

Notes. Multiwavelength data for all of our sources with 24 μm flux density $\gtrsim 1.0$ and $R - [24] \gtrsim 15$. Included are the 11 sources discussed in this paper, the 12 power-law sources, and two additional sources not included in our analysis (15 and 17). Single asterisks (*) indicate where data are probably useless due to nearby contaminating source(s). Double asterisks (**) indicate similar cases where sources were deblended but the uncertainty in measured flux densities is high.

^a H05 indicates sources from Houck et al. (2005); D06 indicates sources from Weedman et al. (2006).

^b SST24 source name derives from discovery with MIPS 24 μm images; coordinates listed are J2000 24 μm positions with typical 3σ uncertainty of $\pm 1''$.

^c IRS spectra ID.

^d The 14–33 μm power-law index (Weedman et al. 2006).

^e Flux densities at 20 cm (de Vries et al. 2002).

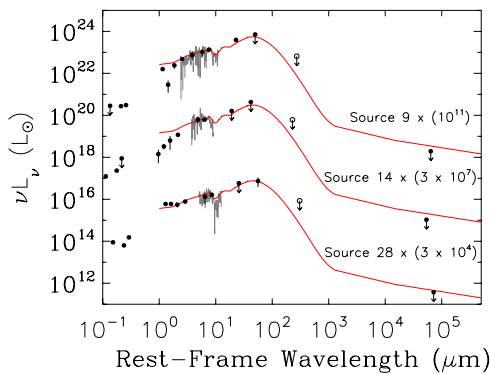


Figure 1. Source SEDs best-fit by Mrk231. Plotted are available data from B_W , R , I , and IRAC bands (3.6, 4.5, 5.8, and 8.0 μm), IRS spectra (including data points at 12 and 18 μm), MIPS bands (24, 70, and 160 μm), 850 μm (calculated from the radio–far-IR relation from the text), and 20 cm. All upper limits (arrows) are plotted at 3σ levels (except for the optical data, which is plotted at 2σ); the error bars shown are 1σ . The sources were fit using the MIPS bands (24, 70, and 160 μm observed-frame) and the IRS 12 and 18 μm data points. Mrk231 provides a good fit for all the sources in the mid- to far-IR regime. This, coupled with the lack of obvious aromatic features, indicates that these sources have a dominant fraction of AGN emission contributing to the overall IR emission.

(A color version of this figure is available in the online journal.)

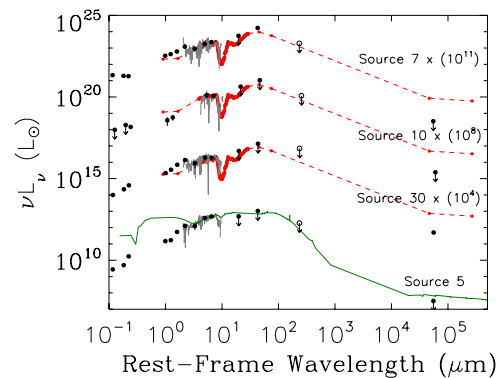


Figure 2. Source SEDs best-fit by F00183–7111 (top three sources, red) and NGC 1068 (bottom source, green). The data are plotted in the same manner as Figure 1. Both templates provide reasonably good fits for the mid- to far-IR regime; the high obscuration of our sources is readily apparent in Source 5 at wavelengths smaller than those covered by the IRS spectrum. As in Figure 1, none of these sources have obvious aromatic features, possibly indicating the dominance of an AGN component over star formation activity, especially with the sources fit by F00183–7111, an AGN-dominated galaxy. However, it is still possible for these sources to have some fraction of star formation contributing to the far-IR emission, especially for Source 5.

(A color version of this figure is available in the online journal.)

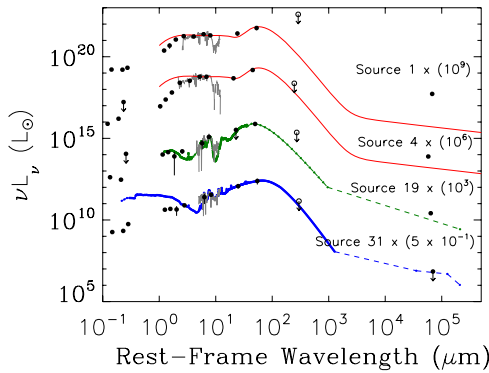


Figure 3. Source SEDs best-fit by CXO J1417 (top two, red), IRAS 1525 (third down, green) and NGC 7714 (bottom, blue). The data are plotted in the same manner as Figure 1. Despite CXO J1417 having approximately half of its IR emission from star formation (and half from an AGN), no aromatic features are present, and the mid-IR SED appears relatively flat and warm, like the sources in Figures 1 and 2. Sources 19 and 31, however, have steeper SEDs and faint aromatic features, and their IRS spectra are vastly different from our other sources. It is apparent that Sources 19 and 31 have much larger fractions of star formation contributing to the far-IR than all of our other objects. The flatness of the source SEDs at rest-frame 1–5 μm suggests that there is still an AGN present and contributing to the warm, mid-IR emission, however.

(A color version of this figure is available in the online journal.)

3.1. Source SEDs and Comparison With Local Analogues

The main questions concerning sources of this nature involve the amount of reprocessed emission in the IR (bolometric IR luminosity) and the origin of said emission (AGN or star formation). One way we can try to answer these questions is to assume our sources are similar to local analogues and compare these local template SEDs to our high-redshift galaxies. While this may not be an accurate assumption, it is difficult to robustly constrain the IR SED shape—and therefore, the contribution of AGN or star formation—without significant IR and submillimeter coverage. Previous analysis of our sample of sources was based on their emission detected at optical and mid-IR wavelengths (Houck et al. 2005). Extrapolations to infer their far-IR, and therefore bolometric, properties were performed at the cost of significant uncertainties, given the large dispersion of mid- to far-IR colors among the most IR luminous galaxies (Armus et al. 2006; Papovich et al. 2007). Here, we use our 70 and 160 μm observations with spectral templates of local analogues to constrain the far-IR properties of our sources and to bring further insight into their nature.

We include the four templates employed by Houck et al. (2005) in their fitting of the mid-IR IRS spectra of their sources: NGC 7714, Arp220, Mrk231, and F00183–7111. NGC 7714 (Dressel & Condon 1978; Brandl et al. 2004; Schmitt et al. 2006; Laine et al. 2006; Marshall et al. 2007) is a “prototypical starburst galaxy” in an interacting system, the SED of which has shallow silicate absorption and a relatively flat far-IR peak. Arp220 (Silva et al. 1998; Imanishi & Dudley 2000; Spoon et al. 2004; Armus et al. 2007) is a well-known, local ULIRG heavily dominated by embedded star formation, as can be seen by its prominent aromatic features and very luminous far-IR peak. Mrk231 (Ivison et al. 2004; Weedman et al. 2005; Armus et al. 2007) is a local AGN (classified as a Seyfert 1) with a relatively flat spectrum and weak aromatic features, though it is known that this source has a nuclear starburst that could contribute significantly to the IR emission. F00183–7111 (Armus et al. 1989; Spoon et al. 2004) is a deeply obscured ULIRG, classified

as a radio-loud LINER/Seyfert ≥ 1.5 . The source is dominated by the AGN in the mid-IR; Spoon et al. (2004) set an upper limit on the IR star-formation component at 30%.

These templates provide star-formation-dominated (NGC 7714) and AGN-dominated (Mrk231, F00183–7111) galaxies, as well as a local ULIRG (Arp220), to compare with our IR-luminous sources. However, many objects have a mix of AGN and star formation contributing to the IR, so we complement the above template set with four more templates: NGC 1068, CXO J1417, NGC 4418, and IRAS 15250+3609. NGC 1068 (Le Flocc’h et al. 2001; Spinoglio et al. 2005) has a Seyfert 2 nucleus with a circumnuclear starburst dominating at mid- and far-IR wavelengths, respectively. CXO J1417 (Le Flocc’h et al. 2007) is a merger system with a bright AGN and star formation contributing comparable emission to the bolometric IR luminosity. NGC 4418 (Spoon et al. 2001; Evans et al. 2003; Imanishi et al. 2004) is a powerful obscured AGN with a possible small amount of star formation contributing to the IR. IRAS 15250+3609 is a very heavily obscured star-forming galaxy, as judged by its lack of high-excitation fine structure lines and minimal X-ray emission (Baan & Klöckner 2006; Armus et al. 2007); however, it has some attributes that in other sources are associated with an AGN: deep silicate absorption without strong accompanying aromatic features and an SED with high output in the mid-IR relative to the far-IR. While IRAS 15250+3609 is not a composite AGN/star-forming galaxy, we include it to account for our strongly absorbed sources with little or no IR emission from an AGN.

To identify local analogues of our sources, we fit these eight templates to our mid- and far-IR data at IRS wavelengths and the MIPS bands (24, 70, and 160 μm). Fitting all the points in the full IRS spectrum with the 70 and 160 μm data would result in fits dominated by the IRS spectrum. Since we wish to focus on the far-IR properties, we select two wavelengths within the IRS spectra to be representative of the continuum emission: observed-frame 12 and 18 μm . (For those sources without IRS data at 12 μm we only used the 18 μm point for the fitting.) We also tested fitting the rest-frame IRAC 8.0 μm point. We decided not to include the IRAC points because this caused the fits to become dominated by the near-IR rather than the far-IR, the latter being more important for determining far-IR luminosities. Because our sources are heavily obscured, the near-IR emission may be significantly attenuated and not provide good fits to the templates. Additionally, we avoid wavelengths affected by the rest-frame 9.7 μm silicate absorption in our fits. The width and depth of the absorption depends on several variables, and it can vary drastically from object to object regardless of AGN strength or amount of star formation (Hao et al. 2007). For example, Mrk231 and F00183–7111 have very similar SEDs in the IR, and both have strong AGN emission; however, Mrk231 has shallow silicate absorption, while F00183–7111 has a deep feature.

Figures 1–3 show the results of the template fitting. We compare the SEDs with all data from optical (B_W , R , and I , where available), IRAC, 12 and 18 μm described in the previous paragraph, IRS spectra, MIPS, 850 μm upper limits calculated from the 20 cm flux density, and the 20 cm flux density itself. Upper limits are plotted at 3σ as arrows (except for the optical data, which is plotted at 2σ); data points are plotted with 1σ error bars. The 850 μm point is plotted with an open symbol since it was calculated rather than measured. The sources in Figure 1 are those best-fit by Mrk231. The fits are within the measurement errors at mid- and far-IR wavelengths (with the exception

of Source 9, where the template slightly underestimates the $70\ \mu\text{m}$ emission). The template also matches the IRS and IRAC wavelengths reasonably well, though the heavy absorption of some of our objects is readily apparent in the IRAC bands (e.g., in Source 14). These indications point to an AGN providing most of the rest-frame mid-IR emission.

Figure 2 shows the sources best-fit by F00183–7111 (top three) and NGC 1068 (bottom). (Data for F00183–7111 are sparse in the submillimeter and radio; therefore, the dashed line should not be misconstrued as representing the SED of this source. To improve the clarity of the plots, a dashed line was used to connect the data points.) As in Figure 1, F00183–7111 and NGC 1068 cover the mid- and far-IR wavelengths with reasonable accuracy. The SEDs of these sources are also characterized by warm colors, flat SEDs, and no obvious aromatic features. It is very probable that star formation is occurring in both these objects and those in the previous figure, but the typical star formation indicators in the mid-IR are drowned out by the AGN. As with the sources in Figure 1, it appears these objects are also dominated by AGN emission in the mid-IR.

Figure 3 shows the sources fit by CXO J1417 (top two), NGC 7714 (third down), and the heavily obscured starburst IRAS 1525 (bottom). (The dashed lines are again used to highlight the available data and not a representation of the actual SEDs of the templates.) Sources 1 and 4 are similar to those in the previous figures: warm SEDs with no obvious aromatic features and absorption taking over at IRAC wavelengths. However, CXO J1417 is known to have equal amounts of AGN and star formation contributing to the mid- and far-IR, respectively, so it is possible for these two objects to have more star formation contributing to the IR emission than the previously mentioned objects. Sources 19 and 31 are unique. Unlike all of our other galaxies, these have steep IRS spectra and faint aromatic features, resulting in good fits with our two star-forming templates, NGC 7714 and IRAS 1525, particularly in both the mid- and far-IR. It is apparent that these two objects have a higher fraction of star formation emitting in the IR than our other sources. (At least, an AGN is not dominating the IR emission.)

Interestingly, all of our sources except for numbers 19 and 31 had similar χ^2 values for the templates with significant AGN emission: Mrk231, F00183–7111, NGC 1068, CXO J1419. Most of our objects exhibit warm SEDs with no obvious aromatic features, indications that an obscured AGN is overpowering any star formation indicators in the near- and mid-IR (Figure 4). Even the two star-forming sources, 19 and 31, do not exhibit a stellar “bump” like typical star-forming objects such as IRAS 1525 and NGC 7714. Indeed, the SEDs remain flat in this part of the spectrum, which indicates that warm dust, presumably heated by an AGN, is contributing at those wavelengths (rest-frame $1\text{--}5\ \mu\text{m}$). We conclude that our sources are characterized by warm dust components reminiscent of an AGN and mid- to far-IR SEDs much shallower than those of typical starburst-dominated ULIRGs at low redshift, though we can only roughly constrain the amount of star formation in any of our sources.

It is interesting that Mrk231 may be a reasonably accurate overall prototype for the majority of our high-redshift sources at mid- and far-IR wavelengths. While only three of our sources were best-fit by Mrk231, F00183–7111 is almost identical from the mid- to far-IR wavelengths, and Mrk231 also fits the three sources where F00183–7111 was preferred (7, 10, and 30)

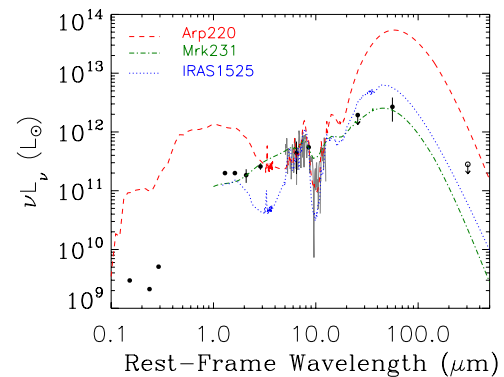


Figure 4. Comparison of Arp220 (red dashed line), Mrk231 (green dot-dashed line), and IRAS 1525 (blue dotted line) matched to the IRS spectrum of Source 28. This object is representative of the majority of our sample: a warm SED with relatively flat far-IR emission, unlike nearby ULIRGs (Arp220) or obscured star-forming galaxies (IRAS 1525).

(A color version of this figure is available in the online journal.)

fairly well, unlike the star-forming templates. Source 5, fit by NGC 1068, and Sources 1 and 4, fit by CXO J1417, give similar results. This would mean that 9 of our 11 sources are reasonably similar to Mrk231. If we look at the entire spectrum of Mrk231 (and if it were placed at $z > 2$), it would pass the $R - [24] \gtrsim 15$ color cut and be included in our sample (Edelson & Malkan 1986, except for being slightly lower in luminosity). The main caveat to using Mrk231 involves the silicate absorption feature, which varies greatly between sources and templates.

Despite the quality of the template fits at mid- and far-IR wavelengths, the 20 cm emission is not as well fit, though some of the poor fits are not surprising. The top three sources in Figure 2 all have far less radio emission than predicted by the template, F00183-7111. The overestimation of the radio is due to the template, which harbors a radio-loud AGN. If we assume our sources include radio-quiet AGNs, then the 20 cm emission makes more sense. The opposite seems to be occurring in the sources we classified as having significant star formation (Figure 3). Considering the $850\ \mu\text{m}$ upper limits are good indicators of the 20 cm emission with respect to the templates, sources 1 and 19 have the largest underestimated radio emission. It is likely that these two sources (and possibly Source 4) have additional radio emission from an AGN that does not exist in pure star-forming galaxies. However, we cannot explain all of our poor radio fits, such as the objects in Figure 1 and Source 5 from Figure 2. ULIRGs (and even submillimeter galaxies, which are thought to be dominated in the IR by star formation) can vary greatly at radio wavelengths, from radio-quiet to radio-loud (Sajina et al. 2008; Pope et al. 2006, so it is possible our poor radio fits are merely due to slight differences from source to source. Also, Houck et al. (2005) show that the radio-IR relation for our objects is similar to starbursts or radio-quiet galaxies. The correlation of our own estimation of the total IR luminosity using the 20 cm emission and other methods (more about this in the following section) confirm that the templates are not too dissimilar to our sources, even in the radio. However, this does tell us that galaxies such as those in our sample are more complicated than normalized versions of typical local analogues, and more research should be done in this area especially at sub-mm and radio wavelengths—in order to better understand the differences between high-redshift ULIRGs/HyLIRGs and similar low-redshift galaxies.

Table 2
 $L_{\text{IR,bol}}$ Estimations

Source	Best-Fit Template	Template $L_{\text{IR,bol}}^{\text{a}}$ (L_{\odot})	Blackbody $L_{\text{IR,bol}}^{\text{b}}$ (L_{\odot})	$L_{\text{IR,bol}}$ (20 cm) ^c (L_{\odot})
1	CXO J1417	1.0×10^{13}	$0.73\text{--}14 \times 10^{13}$	2.0×10^{14}
4	CXO J1417	3.0×10^{13}	$1.9\text{--}3.9 \times 10^{13}$	2.7×10^{13}
5	NGC 1068	2.3×10^{13}	$0.52\text{--}2.6 \times 10^{13}$	$< 1.1 \times 10^{13}$
7	F00183–7111	1.2×10^{13}	$1.7\text{--}4.3 \times 10^{13}$	$< 1.1 \times 10^{13}$
9	Mrk231	8.6×10^{12}	$4.4\text{--}16 \times 10^{12}$	$< 7.1 \times 10^{12}$
10	F00183–7111	6.9×10^{12}	$2.1\text{--}23 \times 10^{12}$	$< 8.8 \times 10^{12}$
14	Mrk231	1.7×10^{13}	$0.32\text{--}3.4 \times 10^{13}$	$< 1.2 \times 10^{13}$
19	IRAS 1525	5.9×10^{12}	$8.2\text{--}30 \times 10^{12}$	9.5×10^{12}
28	Mrk231	4.0×10^{12}	$2.4\text{--}8.3 \times 10^{12}$	$< 4.8 \times 10^{12}$
30	F00183–7111	1.1×10^{13}	$0.39\text{--}6.0 \times 10^{13}$	1.7×10^{13}
31	NGC 7714	8.8×10^{12}	$5.5\text{--}12 \times 10^{12}$	$< 5.3 \times 10^{12}$

Notes. Estimated IR luminosities from fitting templates of nearby sources, blackbody fitting, and 20 cm radio–IR relation.

^a Estimated by integrating under the best-fit template.

^b Rough estimations from matching modified blackbodies to the available data.

^c Estimated from the 20 cm radio flux density from each source.

3.2. IR Bolometric Luminosity

Determining the bolometric IR (8–1000 μm) luminosity of galaxies is important for understanding the underlying source of the IR emission in more detail. For instance, combining the bolometric IR luminosity of a source with the fraction of star formation and/or AGN emission contributing to the IR luminosity allows an estimation of the star formation rate and/or black hole accretion rate, respectively (Merloni & Heinz 2008; Kennicutt 1998).

3.2.1. Luminosity Estimated From Template Fitting

Perhaps one of the easiest ways to estimate the IR bolometric luminosities of our sources is to use the templates discussed in the previous section. The majority of our objects were fit very well with the templates (within errors). We estimated the IR luminosity by multiplying the template IR luminosity by the normalization constant from the template fitting. The results of this method are shown in Table 2. Luminosities range from $\sim 3 \times 10^{12} L_{\odot}$ to $\sim 2 \times 10^{13} L_{\odot}$.

There are several sources of error in this technique, the main arising from our far-IR and submillimeter upper limits. Without detections in these bands, we can only assume that the IR luminosities of our sources follow the template SEDs. There will also be some error in Sources 4, 7, and 9, which have been slightly underestimated by their best-fit templates at 70 and 160 μm .

3.2.2. Luminosity Estimated From Blackbody Fitting

While the template fitting provides us with estimations of the bolometric IR luminosity, it does not let us explore the uncertainties quantitatively. Here, we fit modified blackbodies to our measurements and upper limits to try to evaluate the uncertainties in our bolometric IR luminosity estimations. Our blackbody modeling involves more free parameters than data points, making it inappropriate for deriving dust populations or the exact shape of the far-IR/submillimeter SED. Instead, we are using this procedure only to find reasonable limits on the bolometric IR luminosity.

Assuming that the submillimeter and radio emission are dominated by star formation, we can use the 20 cm measurements

of our sources to calculate the probable 850 μm flux density via a form of the radio-IR relation, as mentioned earlier (Condon 1992; Yun & Carilli 2002; Seymour et al. 2008; Rieke et al. 2009). Given the strong far-IR output relative to the radio for star-forming galaxies compared with that for AGN, as well as that most of our sources have only upper limits at 20 cm, we can safely interpret the estimates as upper limits. This radio-IR relation, of course, does not hold for radio-loud AGN, of which we have one: Source 1. As such, the 850 μm upper limit for this source is an extreme and very conservative limit. We translated all of our 850 μm calculations into 3σ upper limits using standard error propagation techniques.

Even with the submillimeter upper limit, we do not know other properties of the dust, such as emissivity, that can affect any calculation of the IR luminosity. However, we can still use multiple blackbody curves to get a reasonable estimation of the bolometric IR luminosity. We use three modified blackbodies with a dust emissivity wavelength dependence proportional to $\lambda^{-\beta}$ with $\beta = 1.5$ (varying β did not significantly affect the results). We started by setting the coldest blackbody curve at a specific, unvarying temperature and stepping the other two curves through a range of temperatures appropriate to the mid-IR. The summed curve was allowed to vary within the error bars of the 70 and 160 μm data, between 2σ and 3σ below the upper limits (70, 160, and 850 μm), and within the endpoints of the IRS spectra. We calculated L_{bol} for each set of temperatures and selected the minimum and maximum resulting in a realistic SED curve that reasonably fit the data and the continuum of the IRS spectra. Selecting the minima was straightforward: we simply chose the fit that resulted in a minimum L_{bol} (within the above constraints). The only caveat concerns the sources for which we only have upper limits at 70 and 160 μm . Without at least one detection at these bands, we cannot robustly constrain the minimum. Given the shape of our SEDs, however, the minima are reasonable. Estimating the maxima was a little more tricky. Many of the sources, when fit with the coldest blackbody set to 20 K, resulted in $L_{\text{bol}} \sim 10^{14} L_{\odot}$, resembling or exceeding the far-IR peak of Arp220. Such high luminosities are unlikely, and we do not consider such fits to result in “realistic” SED curves. Our stated maxima L_{bol} , then, are chosen to represent more typical far-IR SEDs than sources such as Arp220. This means

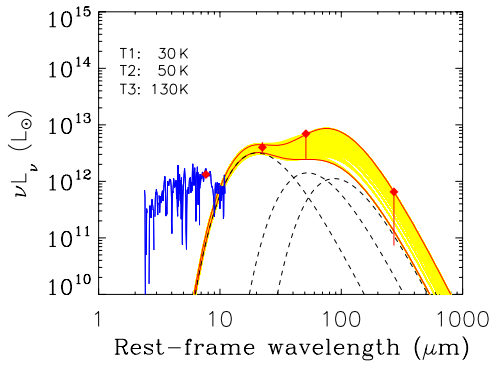


Figure 5. Example of our blackbody fitting for Source 9 resulting in the minimum value for the bolometric IR luminosity. Plotted with the SED are the blackbody curves with their respective temperatures (dashed lines), all possible fits given the limitations discussed in the text (yellow in the color figure), and the minimum (maximum) bolometric IR luminosity shown by the lower (upper) solid lines, respectively (red in the color figure). Please note that while the maximum L_{bol} fit shown is the overall maximum for this source (listed in Table 2), the minimum L_{bol} shown is the minimum for this particular set of blackbody curves. It is not the overall minimum (listed in Table 2).

(A color version of this figure is available in the online journal.)

our upper limits are estimates, and there may be significant errors associated with them.

An example of our blackbody fitting technique is shown in Figure 5. The SED of Source 9 is plotted, along with the blackbodies and their respective temperatures (dashed lines), all possible fits given the limitations discussed above (yellow in the color figure), and the minimum (maximum) L_{bol} for this particular fit, denoted by the solid lower (upper) lines, respectively (red in the color figure). The upper solid line in this figure denotes the blackbody fit for the overall maximum L_{bol} for this particular source (listed in Table 2). Please note that the minimum shown is not the overall minimum given in the table.

In addition to the L_{bol} estimated from our template fitting, we also compared our bolometric luminosities with the IR luminosity calculated from the 20 cm flux density using the relations in Helou et al. (1985) and Condon (1992). These relations strictly apply only for star-forming galaxies and therefore probably overestimate the far-IR for many of our sources. The results are listed in Table 2. The IR bolometric luminosity minima and maxima calculated from the blackbody fitting are consistent with both the best-fit template luminosities and the 20 cm luminosities with few exceptions. Not surprisingly, the most notable exception is the radio-loud Source 1, which has a higher L_{IR} from the 20 cm flux density than we estimated using modified blackbodies. All sources (using all techniques) range from a few times $10^{12} L_{\odot}$ to a few times $10^{13} L_{\odot}$. Tighter constraints on L_{IR} would be possible with observations that better constrain the far-IR peak in the SED. These high bolometric luminosities support our conclusions from the previous section: most of our sources are dominated by obscured AGN emission in the mid-IR rather than star formation.

4. DISCUSSION

Our template comparisons reinforce previous findings (Houck et al. 2005; Yan et al. 2005; Brand et al. 2007; Dey et al. 2008; Fiore et al. 2008) that these sources, at the very least, have significant AGN emission powering the IR output. A few of the sources have indicators of star formation contributing to the far-IR emission; two of these sources also have faint aromatic

features. However, even in the star-forming objects, there is evidence for AGN, and in the majority, the AGN is strong enough to wash out most indicators of the star-formation activity. We can compare our objects to the de Grijp et al. (1987) classification of IRAS sources. The authors define “warm,” AGN-like colors to be in the range $-1.5 \lesssim \alpha(25, 60) \lesssim 0.0$, where $\alpha(25, 60)$ is the spectral index between the 25 and 60 μm flux densities using the conversion $F_{\nu} \propto \nu^{\alpha}$. We calculated the equivalent IRAS 25/IRAS 60 colors from the MIPS 70/MIPS 160 measurements, which is a reasonable estimation since our sources are at $z \sim 2$. The original 11 sources have spectral indices of $-1.2 \lesssim \alpha \lesssim -0.78$, easily falling into the warm, AGN-like color range.

It is possible to create a warm SED (like our sources) using star formation alone, but this requires an atypical dust distribution with most of the obscuring material very near to a nuclear starburst. This could result in objects with warmer than expected IR emission and subdued far-IR. However, such objects would still have a cold dust peak more similar to what we expect for obscured star-forming galaxies. Even with a warm dust component from a central starburst, we would also expect to see stronger aromatic features. While we cannot completely rule out the possibility, there is little evidence from our data that these objects are dominated by star formation.

This conclusion—that AGNs provide a significant amount of IR output in these sources—is strengthened if we take into account the 12 power-law sources. At IRS wavelengths, these objects appear identical to pure AGN; there are no obvious features in the spectra, like aromatic emission or silicate absorption. It is plausible that most of the power-law sources are at similar distances as the sources with known redshifts (e.g., Desai et al. 2008). Some may even be at higher redshift, so the mid-IR features are redshifted out of the IRS range. However, Donley et al. (2007) show that even an extreme object similar to Arp220 would appear to be a power-law source at $z = 2.8$ only if $L_{\text{bol}} \gtrsim 2.0 \times 10^{13} L_{\odot}$. It would probably require a significant fraction of IR emission from an embedded AGN to reach such high luminosities. Assuming the majority of the pure power-law sources are at similar redshifts as the ones with spectral features, as many as 20 of the 23 objects in our sample have their rest mid-IR emission (5–20 μm) dominated by the AGN.

It is still unknown, however, what role in galactic evolution these objects play. If the AGN activity and feedback do indeed stifle star formation, this class of object could give us information on when these sources ceased the large-scale star formation. Perhaps we are looking at a time in galaxy evolution where the AGN in these galaxies have turned on and are suppressing the star formation, resulting in objects with strong AGN emission and comparatively low levels of star formation. It is also possible that the star formation occurring in these sources is either enhanced by the AGN or mostly unrelated to the AGN. Additionally, the apparent AGN activity may be transient, and we are seeing a brief period in the evolution of these objects.

5. CONCLUSIONS

We have determined the AGN content of a sample of 20 luminous IR galaxies from Houck et al. (2005) using the MIPS 70 and 160 μm arrays on *Spitzer*. These galaxies are extreme examples of the class of dust-obscured galaxies (e.g., Fiore et al. 2008; Dey et al. 2008) with $R - [24] > 15$ and $F_{24} \gtrsim 1$ mJy. We computed SEDs for 11 of these sources from optical-to-radio wavelengths and fit templates of nearby analogues to our SEDs to estimate their IR luminosities and to study the possible

mechanisms for this emission. Our sources are classified as ULIRGs and HyLIRGs, with consistent luminosities estimated from three different methods and ranging from $4 \times 10^{12} L_{\odot} \lesssim L_{\text{IR}} \lesssim 3 \times 10^{13} L_{\odot}$. Our objects are characterized by warm dust, flat far-IR SEDs, and few (if any) aromatic features, more closely matching AGN-dominated local analogues than star-forming systems. These lead us to conclude that most of our sources contain an AGN that contributes significantly to the IR output, probably dominating it in many cases. Only a few sources have star formation activity at a level that makes it apparent in their mid-IR spectra or far-IR SEDs.

We thank all of our MIPS, IRS, and Boötes collaborators for their discussion and input, as well as Jason Marshall for supplying us with the NGC 7714 template and the referee for useful comments and suggestions. This work is based on observations made with the *Spitzer Space Telescope*, which is operated by NASA/JPL/Caltech. We thank NASA for financial support through contracts 1255094 and 1276199. E.L.F. and C.P. acknowledge support by NASA through the *Spitzer Space Telescope* Fellowship Program. The research activities of A.D. and B.T.J. are supported by NAO, which is operated by the Association of Universities for Research in Astronomy (AURA) under a cooperative agreement with the National Science Foundation. V.C. acknowledges partial support from the EU ToK grant 39965.

REFERENCES

- Alonso-Herrero, A., et al. 2006, *ApJ*, **640**, 167
 Armus, L., Heckman, T. M., & Miley, G. K. 1989, *ApJ*, **347**, 727
 Armus, L., et al. 2006, *ApJ*, **640**, 204
 Armus, L., et al. 2007, *ApJ*, **656**, 148
 Aussel, H., Elbaz, D., Cesarsky, C. J., & Starck, J. L. 1999, *Ap&SS*, **266**, 307
 Baan, W. A., & Klöckner, H.-R. 2006, *A&A*, **449**, 559
 Blain, A. W., Kneib, J.-P., Ivison, R. J., & Smail, I. 1999, *ApJ*, **512**, 87
 Blain, A. W., Smail, I., Ivison, R. J., Kneib, J.-P., & Frayer, D. T. 2002, *Phys. Rep.*, **369**, 111
 Brand, K., et al. 2007, *ApJ*, **663**, 204
 Brandl, B. R., et al. 2004, *ApJS*, **154**, 188
 Brown, M. J. I., et al. 2007, *ApJ*, **654**, 858
 Chapman, S., Blain, A., Ivison, R., & Smail, I. 2003, *Nature*, **422**, 695
 Chapman, S. C., Blain, A. W., Smail, I., & Ivison, R. J. 2005, *ApJ*, **622**, 772
 Chary, R., & Elbaz, D. 2001, *ApJ*, **556**, 562
 Condon, J. J. 1992, *ARA&A*, **30**, 575
 de Grijs, M. H. K., Lub, J., & Miley, G. K. 1987, *A&AS*, **70**, 95
 Desai, V., et al. 2008, *ApJ*, **679**, 1204
 de Vries, W. H., Morganti, R., Röttgering, H. J. A., Vermeulen, R., van Breugel, W., Rengelink, R., & Jarvis, M. J. 2002, *AJ*, **123**, 1784
 Dey, A., et al. 2008, *ApJ*, **677**, 943
 Dole, H., et al. 2001, *A&A*, **372**, 364
 Donley, J. L., Rieke, G. H., Pérez-González, P. G., Rigby, J. R., & Alonso-Herrero, A. 2007, *ApJ*, **660**, 167
 Donley, J. L., Rieke, G. H., Rigby, J. R., & Pérez-González, P. G. 2005, *ApJ*, **634**, 169
 Dressel, L. L., & Condon, J. J. 1978, *ApJS*, **36**, 53
 Edelson, R. A., & Malkan, M. A. 1986, *ApJ*, **308**, 59
 Egami, E., et al. 2004, *ApJS*, **154**, 130
 Eisenhardt, P. R., et al. 2004, *ApJS*, **154**, 48
 Elbaz, D., et al. 1999, *A&A*, **351**, 37
 Evans, A. S., et al. 2003, *AJ*, **125**, 2341
 Farrah, D., Alfonso, J., Efstathiou, A., Rowan-Robinson, M., Fox, M., & Clements, D. 2003, *MNRAS*, **343**, 585
 Fiore, F., et al. 2008, *ApJ*, **672**, 94
 Flores, H., et al. 1999, *ApJ*, **517**, 148
 Franceschini, A., Aussel, H., Cesarsky, C. J., Elbaz, D., & Fadda, D. 2001, *A&A*, **378**, 1
 Gordon, K. D., et al. 2007, *PASP*, **119**, 1019
 Hao, L., Weedman, D. W., Spoon, H. W. W., Marshall, J. A., Levenson, N. A., Elitzur, M., & Houck, J. R. 2007, *ApJ*, **655**, 77
 Helou, G., Soifer, B. T., & Rowan-Robinson, M. 1985, *ApJ*, **298**, 7
 Houck, J. R., et al. 2004, *ApJS*, **154**, 18
 Houck, J. R., et al. 2005, *ApJ*, **622**, 105
 Imanishi, M., & Dudley, C. C. 2000, *ApJ*, **545**, 701
 Imanishi, M., Nakanishi, K., Kuno, N., & Kohno, K. 2004, *AJ*, **128**, 2037
 Ivison, R. J., et al. 2004, *ApJS*, **154**, 124
 Jannuzi, B. T., & Dey, A. 1999, in ASP Conf. Ser. 191, Photometric Redshifts and the Detection of High Redshift Galaxies, ed. R. J. Weymann et al. (San Francisco, CA: ASP), **111**
 Kennicutt, R. C. 1998, *ARA&A*, **36**, 189
 Lacy, M., et al. 2004, *ApJS*, **154**, 166
 Lagache, G., Dole, H., & Puget, J.-L. 2003, *MNRAS*, **338**, 555
 Laine, S., Kotilainen, J. K., Reunanen, J., Ryder, S. D., & Beck, R. 2006, *AJ*, **131**, 701
 Le Floc'h, E., Mirabel, I. F., Laurent, O., Charmandaris, V., Gallais, P., Sauvage, M., Vigroux, L., & Cesarsky, C. 2001, *A&A*, **367**, 487
 Le Floc'h, E., et al. 2005, *ApJ*, **632**, 169
 Le Floc'h, E., et al. 2007, *ApJ*, **660**, 65
 Marshall, J. A., Herter, T. L., Armus, L., Charmandaris, V., Spoon, H. W. W., Bernard-Salas, J., & Houck, J. R. 2007, *ApJ*, **670**, 129
 Merloni, A., & Heinz, S. 2008, *MNRAS*, **388**, 1011
 Papovich, C., et al. 2007, *ApJ*, **668**, 45
 Polletta, M., et al. 2006, *ApJ*, **642**, 673
 Pope, A., et al. 2006, *MNRAS*, **370**, 1185
 Rieke, G. H., & Low, F. J. 1972, *ApJ*, **176**, 95
 Rieke, G. H., et al. 2004, *ApJS*, **154**, 25
 Rieke, G. H., et al. 2009, *ApJ*, in press, arXiv:0810.4150
 Sajina, A., et al. 2008, *ApJ*, **683**, 659
 Schmitt, H. R., Calzetti, D., Armus, L., Giavalisco, M., Heckman, T. M., Kennicutt, R. C., Jr., Leitherer, C., & Meurer, G. R. 2006, *ApJS*, **164**, 52
 Serjeant, S., et al. 2004, *MNRAS*, **355**, 813
 Seymour, N., et al. 2008, *MNRAS*, **386**, 1695
 Silva, L., Granato, G. L., Bressan, A., & Danese, L. 1998, *ApJ*, **509**, 103
 Smail, I., Ivison, R. J., & Blain, A. W. 1997, *ApJ*, **490**, 5
 Soifer, B. T., Neugebauer, G., & Houck, J. R. 1987, *ARA&A*, **25**, 187
 Spinoglio, L., Malkan, M. A., Smith, H. A., González-Alfonso, E., & Fischer, J. 2005, *ApJ*, **623**, 123
 Spoon, H. W. W., Keane, J. V., Tielens, A. G. G. M., Lutz, D., & Moorwood, A. F. M. 2001, *A&A*, **365**, 353
 Spoon, H. W. W., et al. 2004, *ApJS*, **154**, 184
 Stansberry, J. A., et al. 2007, *PASP*, **119**, 1038
 Stern, D., et al. 2005, *ApJ*, **631**, 163
 Weedman, D. W., et al. 2005, *ApJ*, **633**, 706
 Weedman, D. W., et al. 2006, *ApJ*, **651**, 101
 Werner, M. W., et al. 2004, *ApJS*, **154**, 1
 Yan, L., et al. 2004, *ApJS*, **154**, 60
 Yan, L., et al. 2005, *ApJ*, **628**, 604
 Yun, M. S., & Carilli, C. L. 2002, *ApJ*, **568**, 88